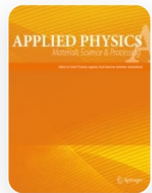# SPRINGER LINK

Log in

☰ Menu   🔍 Search

🛒 Cart

Intensive analysis of uncoated and surface modified Co–Zn nanoferrite as a heat generator in magnetic fluid hyperthermia applications

Download PDF ⤓

Applied Physics A

Aims and scope

Submit manuscript

Deepali D. Andhare ✉, Supriya R. Patade, Mangesh V. Khedkar, Asha A. Nawpute & K. M. Jadhav

Abstract

This article describes structural, morphological, magnetic, and hyperthermia studies of uncoated and polyethylene glycol (PEG) coated zinc substituted cobalt ferrite nanoparticles. The zinc-substituted cobalt nanoparticles were successfully synthesized by the chemical co-precipitation method and the surface of particles coated by PEG showed enhanced the

properties from uncoated nanoparticles. Rietveld refined XRD pattern revealed the formation of cubic spinel structure with Fd-3 m space group. The crystallite size obtained using the Scherrer formula from the XRD pattern and W−H method was found to be highly similar. Raman spectroscopy result suggests the confirmation of spinel phase of prepared sample from the investigation of vibration modes with the help of best-fitting procedure. FTIR study reveals the PEG perfectly coated on prepared nanoparticles which is confirmed by the presence of absorption bands in FTIR spectra. The average particle size calculated from the TEM image was found to be 31 nm which is in good agreement with the crystallite size obtained from XRD. The hydrophilic nature of coated nanoparticles was confirmed from contact angle measurement. The M-H curve and M-T plot revealed the prepared nanoparticles have superparamagnetic nature. The uncoated and coated Co-Zn nanoparticles were dispersed in water base fluid for the magnetic induction heating study. The magnetic hyperthermia application was successfully studied by an induction heating system. The specific absorption rate (SAR) depended on the concentration of nanoparticles and coated nanoparticles show superior SAR values as compared to uncoated nanoparticles. This study concluded that prepared nanoparticles are a promising material for magnetic hyperthermia application for cancer treatment.

Similar content being viewed by others
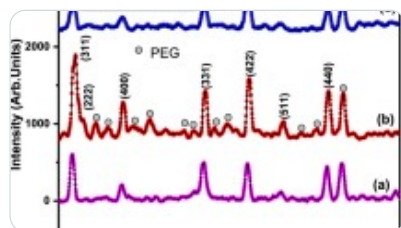
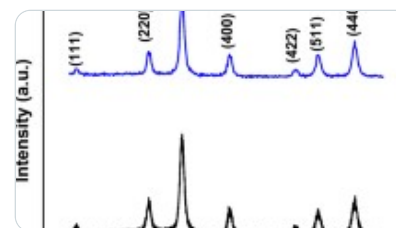**Polyethylene glycol capped nickel−zinc ferrite nanocomposites: structural, optical and...**

Article │ 19 November 2022
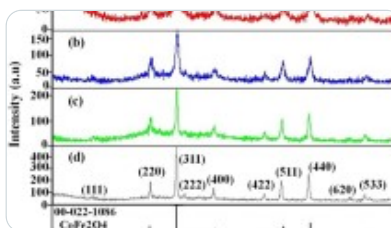
Influence of calcination parameters on the microstructure, magnetic and hyperthermia...

Article │ 05 April 2022

Magnetic Evaluation of the Nanoparticles Coated with Polyvinylpyrrolidone and Polyvinyl Chloride...

Article │ 06 November 2018

Use our pre-submission checklist →

Avoid common mistakes on your manuscript.

1 Introduction

The use of magnetic nanoparticles (NPs) in the biomedical field has been widely increased in recent years. Today's research focused on the design and development of magnetic NPs and increases their applicability in a different field. In the family of spinel ferrite, cobalt ferrite has excellent structural and magnetic properties. It shows moderate saturation magnetization, large magnetostrictive coefficient, high Curie temperature, and high coercivity [1]. Doping by divalent metal ions such as Zn^{2+}, Ni^{2+} and Cd^{2+} reduce its coercivity [2], magnetization [3], and toxicity[4] which results in materials showing ideal properties that are suitable for biomedical applications [5]. The enhanced magnetic and structural properties of Zn doped cobalt ferrite make it an ideal material in a biomedical field such as for drug delivery, biosensors, magnetic resonance imaging, and magnetic hyperthermia applications [6, 7]. $Co_{1-x}Zn_xFe_2O_4$ NPs have been synthesized by various methods like thermal decomposition, Sol−gel auto-combustion, hydrothermal, emulsion and co-precipitation methods [8, 9]. Amongst these, the researcher has a huge interest in the co-precipitation method due to its simple experimental setup, convenient processing, and considerable time-saving properties. Chemotherapy, surgery, radiotherapy, and hyperthermia are some cancer treatments. Amongst these hyperthermia has drawn attention due to negligible side effects [10]. The term hyperthermia is invented from two words 'hyper' and 'therm' it means 'rise' and 'heat' respectively. In another way, the heating of definite tissues or organs to kill cancerous cells by the effect of certain anticancer drugs and radiation is known as hyperthermia [11]. Several ways have been used to induce hyperthermia in the affected region (tumor), but it also affects healthy tissues. In magnetic hyperthermia, magnetic NPs under an external magnetic field are injected via the local region to generate heat in the area of infected cells. Cancerous tissues have very reduced thermal resistance compared to normal tissues because of the poor development of blood vessels in the cancerous tissues. This resulted in the cancerous cells kill within the temperature range of 42−46 °C [12,13,14,15]. The main effective parameter in induction heating study is Specific absorption rate (SAR) which depends on various parameters such as concentration of sample and magnetic property of the sample [16,17,18]. In the last few decades, the interest of researchers in the synthesis and characterization of

magnetic nanoparticles for biomedical application was increased. Recently, Suman et. al [19]. investigated the induction heating properties of surface-modified Cobalt zinc ferrite NPs and effect of annealing temperature. They reported the heating efficiency increased according to annealing temperature and concentration of NPs. Hyunkyung et. al. [20] synthesized Co-Zn ferrite NPs by high-temperature thermal decomposition method and studied their structural, magnetic and hyperthermia properties. They reported the prepared NPs to have excellent magnetic and thermal properties, further these were used for plasma treatment for 30 min which revealed increased hyperfine field. Mohamed et. al. [21] investigated the zinc ferrite and cobalt ferrite NPs synthesized by the conventional co-precipitation method. The SLP was found to be enhanced with respect to concentration, time, medium viscosity and magnetic field strength. Prepared NPs have high SLP value and these are becoming promising material for magnetic hyperthermia.

Coating the core of NPs enhances their properties which are essential for biomedical applications. The coating of NPs reduces particle–particle agglomeration which is helpful to obtain superior SAR value. Somvanshi et. al. [22] reported on the comparative study of pure zinc ferrite and oleic acid-coated zinc ferrite nanoparticles synthesized via the sol–gel method for magnetic hyperthermia application. The coated NPs showed superior SAR value. Amongst coating materials like oleic acid, polyethylene glycol (PEG), chitosan, polyvinyl pyrrolidone, silica, etc. PEG is a promising coater because of its non-toxicity, biocompatibility, and hydrophilic nature. Coaters play the important role in reducing the toxicity of magnetic NPs [23]. The motivation behind the selection of Zn doped Co-ferrite and polyethylene glycol as a coating agent: (1) Zn divalent transition metal was selected as a substituting element because of magnetic properties of cobalt ferrites is sensitive to the Zn metal. (2) The non-magnetic Zn reduces the magnetization of cobalt ferrite and obtained the superparamagnetic nature which is an essential condition in magnetic hyperthermia application study. (3) PEG has demonstrated to be an excellent NPs stabilizer and improves the hydrophilicity of NPs which results the enhanced magnetic hyperthermia properties. (4) Only few articles are available on the PEG coated Zn doped Co-ferrite nanoparticles and its biomedical application.

In the present report, $Co_{0.7}Zn_{0.3}Fe_2O_4$ NPs were synthesized by a cost-effective chemical co-precipitation route, after which their surfaces were modified by coating with PEG. Prepared NPs characterized by different characterization techniques. The impact of PEG coating on

magnetic hyperthermia detailed study was investigated using an induction heating system. We believe that the present research work is relevant to the development of nanoparticles with improved structural, morphological, magnetic and hyperthermia, etc. properties that it represents a breakthrough in nanomaterials approaches towards biomedical application specially for magnetic hyperthermia.

2 Experimental

2.1 Materials and methods

$Co_{0.7}Zn_{0.3}Fe_2O_4$ NPs were synthesized by the Co-precipitation method. The zinc chloride ($ZnCl_2$), cobalt chloride hexahydrate ($CoCl_2.6H_2O$), ferric chloride ($FeCl_3$), polyethylene glycol ($H(OCH_2)_nCH_2OH$) for surface modification of NPs and NaOH for maintaining pH (all these chemicals are AR grade) were used for the synthesis of $Co_{0.7}Zn_{0.3}Fe_2O_4$ NPs. The molar solution with a proportionality ratio of $CoCl_2.6H_2O$: $ZnCl_2$: $FeCl_3$ was 0.7:0.3:2 mixed together at room temperature under constant stirring at 300 rpm for 30 min. A 1 M NaOH was added drop-wise to maintain the pH of solution 9. Then increased the temperature of the solution up to 80 °C and kept it at a constant stirring 300 rpm for 2 h to form precipitation. The precipitate was washed several times with hot distilled water and dry NPs at room temperature for 48 h. After being grounded, the prepared powder was sintered at 600 °C for 6 h. The synthesized NPs were characterized by different characterization techniques. The prepared $Co_{0.7}Zn_{0.3}Fe_2O_4$ NPs were labeled as 'CZF'.

2.1.1 Preparation of PEG-coated NPs

The 20 mg of prepared $Co_{0.7}Zn_{0.3}Fe_2O_4$ NPs and an equal amount of PEG were dispersed in DI water separately and stirred for 20 min. Then polymer solution was added drop-wise in NPs dispersed solution and stirred this solution for 3 h. After that, properly coated NPs were washed several times with DI water and dried at room temperature for 48 h. The prepared NPs were labeled as 'PEG-CZF' and used for further characterization. The coating procedure is illustrated and explained in detail in Fig. 1.

Fig. 1
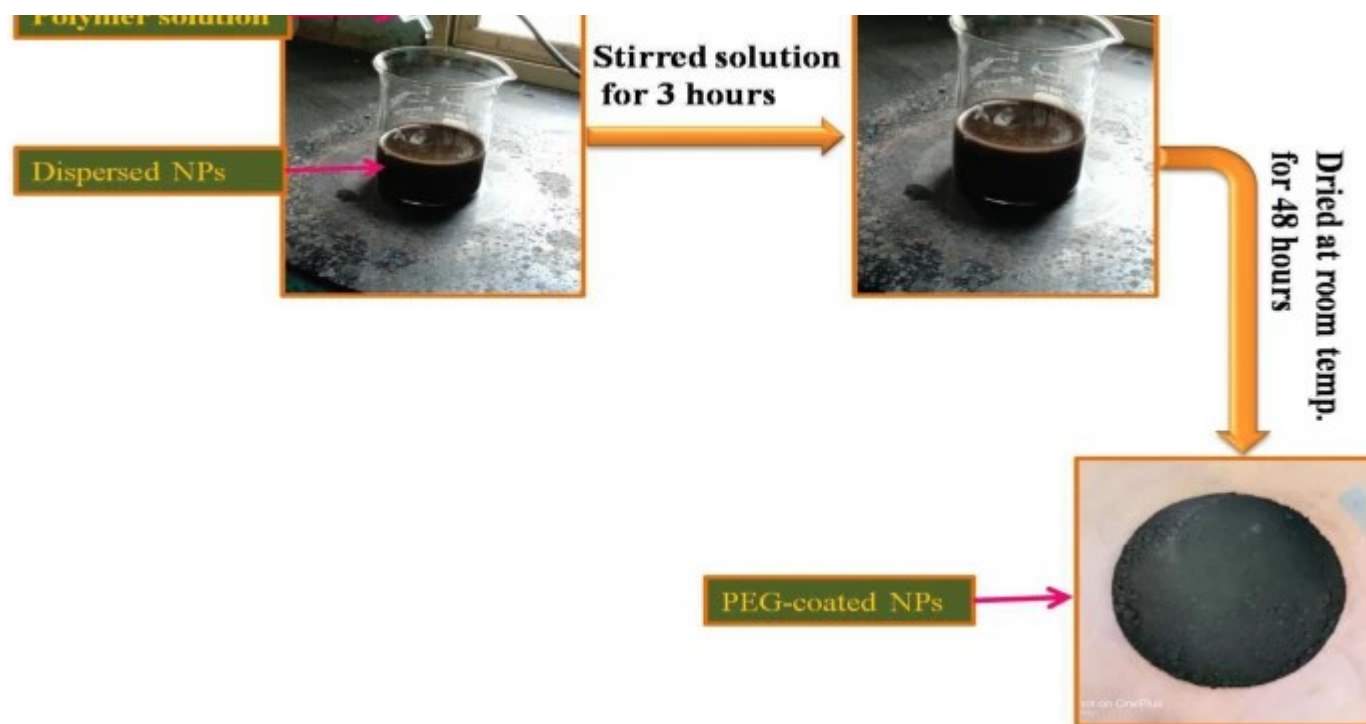
Schematic representation of the coating of $Co_{0.7}Zn_{0.3}Fe_2O_4$ NPs

2.2 Characterizations

The details about characterizations, instrument name, conditions during measurement are shown in Table 1.

Table 1 Characterization details (here *RT* Room temperature, *AMF* applied magnetic field, *FR* frequency range, *WR* wavenumber range)

3 Results and discussion

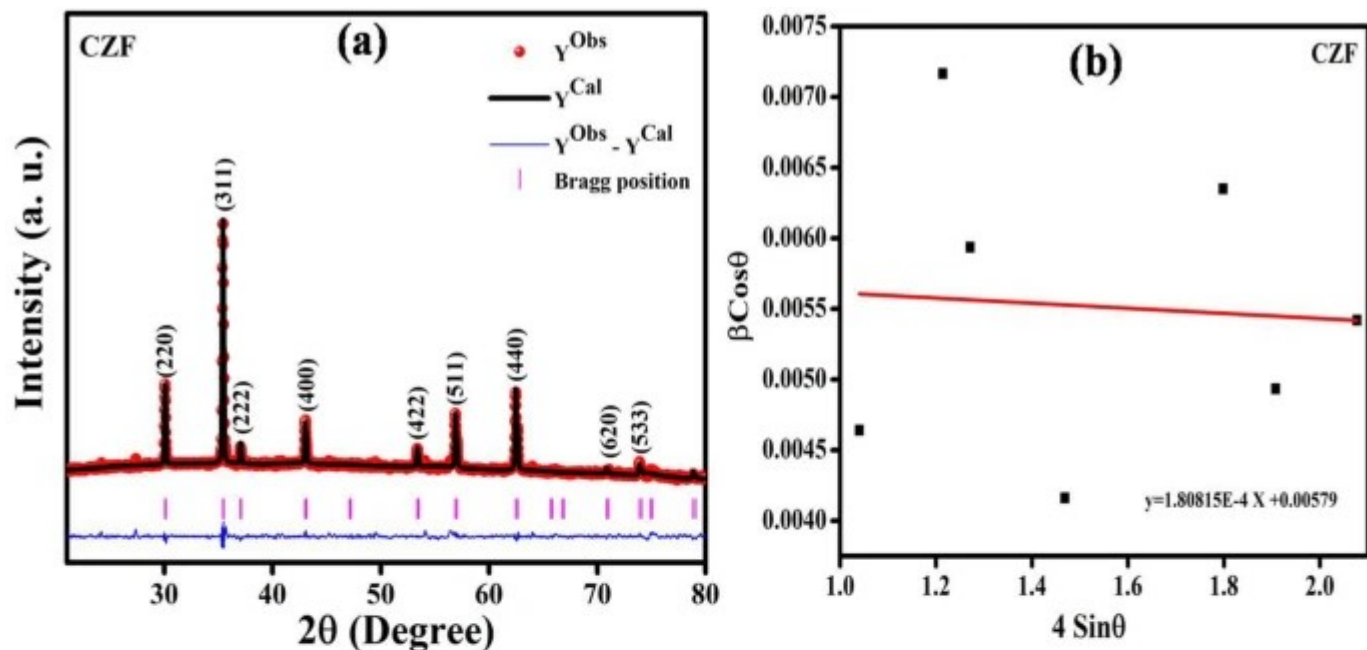### 3.1 Structural and elemental properties

Figure 2(a) represents the Rietveld refined pattern of XRD data of CZF NPs which was performed using FullProf Suite software. The black-colored line represents the calculated intensity and the red-colored dots represent the experimental intensity. Bragg's positions
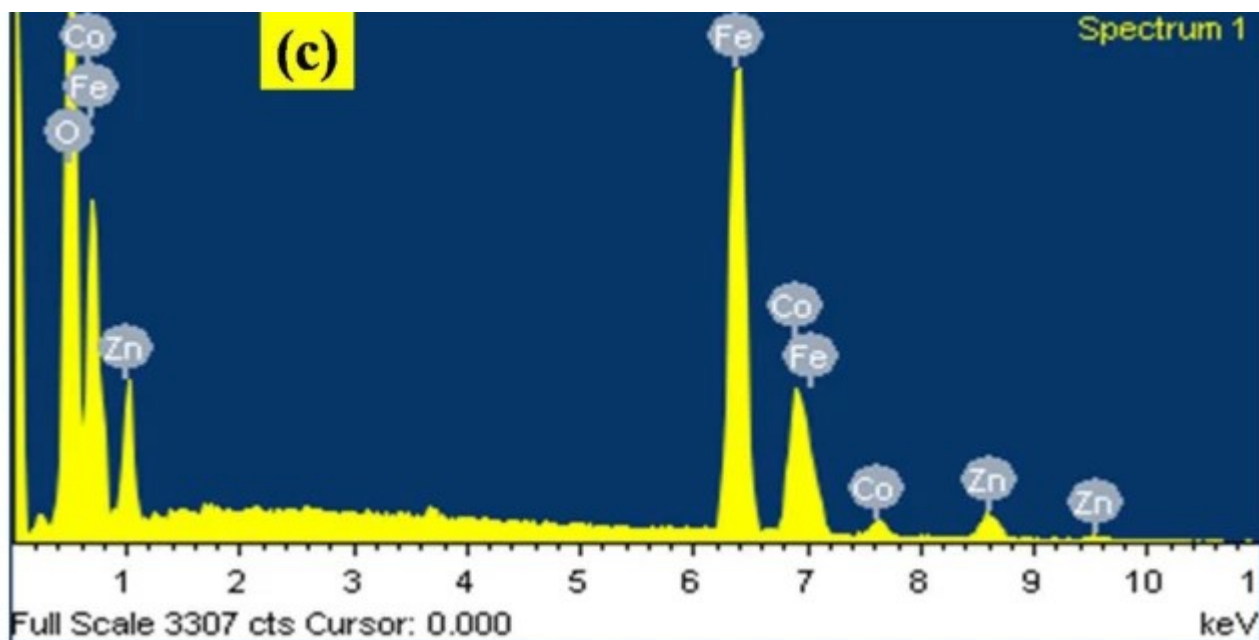
signify the Fd−3 m space group shown at the bottom by vertical lines. The difference between the measured and calculated intensity level is shown at the bottom as a blue-colored line. The reflection planes which have (h k l) values indicated in the XRD pattern revealed the formation of cubic spinel structure with Fd−3 m space group. There is no impurity peak observed in a pattern which indicates the high purity of the sample. This was also confirmed from the EDS spectra of the CZF sample shown in Fig. 2 (c). The XRD pattern of the prepared sample was well refined which was confirmed by the refinement factors like $\chi2$, R_p, R_{wp} and $R_{exp.}$ The refinement factors indicate the quality of refinement. The value of $\chi2$ was found to be very close to the one, this is a sign of good quality. All refinement factors are tabulated in Table 2 The other structural parameters such as a_{Rt}, D_{W-H}, d_x, d_B, P(%), r_A and r_B were calculated from the XRD pattern, shown in Table 2. The structural parameters were calculated with the help of lattice parameter values. The crystallite size of the prepared sample at 24 nm was calculated using the Debye−Scherrer's formula

$$ D = {\raise0.7ex\hbox{${k\lambda }$} \!\mathord{\left/ {\vphantom {{k\lambda } {\left({\beta \cos \theta } \right)}}}\right.\kern-\nulldelimiterspace} \!\lower0.7ex\hbox{${\left({\beta \cos \theta } \right)}$}} $$

(1)

Fig. 2

a Rietveld refined XRD pattern, b Williamson − Hall plot and c EDS spectra of CZF

Table 2 Rietveld refinement factors; Profile factor (R_p), Weighted profile factor (R_{wp}), $\chi 2$ and Expected R-factor (R_{exp}), lattice constant (a_{Rt}), D_{S-F}(nm) and D_{W-H} crystallite size calculated by Scherrer's and W−H method respectively, X-ray density 'd_x' (g/cm^3), Bulk density 'd_B'(g/cm^3), Porosity (%) and ionic radii (r_A, r_B) for CZF sample

where D indicates the crystallite size, λ is the X-ray wavelength, k is a constant (value of k is 0.9), β is the full width at half maximum (FWHM) and θ is the diffraction angle.

The X-ray density was calculated using lattice constant value 'a' from Eq. 2.

$$ d_{x} = 8M/\left({N_{A} a^{3} } \right) $$

(2)

where d_x is the X-ray density, M is the molecular weight, 'a' is the lattice constant and N_A is the Avogadro's number. The X-ray density was found to be 5.292 g/cm^3. Using the Archimedes

principle, the bulk density of prepared NP$_S$ was calculated and it was found in the order of 3.721 gm/cm^3. The percentage porosity (P %) was calculated by using both X-ray density and bulk density by using the Eq. (3) and it was observed 29.62%.

$$ P\left(\% \right) = 1 - \left({d_{B} /d_{x} } \right) $$

(3)

The A-site and B-site ionic radii of the prepared sample were found to be 0.5870 Å and 0.7307 Å, respectively, which was calculated from the following Eqs. 4 and 5, respectively. The standard value (i.e. u = 0.0375 nm) of the oxygen positional parameter was used for the calculations of

$$ r_{A} = \left({u - 1/4} \right)a\sqrt 3 - r\left({O^{2 - } } \right) $$

(4)

$$ r_{B} = \left({5/8 - u} \right) - r\left({O^{2 - } } \right) $$

(5)

Methods such as the Warren−Averbach method and Williamsons Hall method can give clear information about the microstructure of the lattice and its intrinsic strain. Williamson–Hall (W−H) method is very simple and easy to use to calculate the structural parameters. In the present study, we have calculated the average particle size and microstrain by using the uniform deformation model (UDM). The total broadening of X-ray diffraction peaks which have hkl values due to the microstrain and size of nanocrystals can be expressed by the equation

$$ \beta_{{{\text{hkl}}}} = \beta_{{{\text{size}}}} + \beta_{{{\text{strain}}}} $$

(6)

where β_{hkl} is the full width at half maxima of different diffraction planes. Figure 2 (b) Shows

the plotting based on Eq. 6 with the term $\beta\,Cos\theta$ on the y-axis and $4Sin\theta$ on the x-axis, this is the good fitted straight line. The slope of this line gives the value of intrinsic strain i.e. 1.808×10^{-4}. The crystallite size (D_{W-H}) calculated from the UDM was found to be 23.94 nm, which is nearly the same as that of crystallite size (D_{S-F}) calculated from the Debye–Scherrer's formula [24]. Crystallite sizes calculated from both methods are given in Table 2 comparatively. The purity of the chemical composition of the sample was further investigated using the energy-dispersive X-ray spectroscopy (EDS) technique, as shown in Fig. 2(c) for the CZF sample. The EDS plot indicates the sample CZF was composed of Co, Zn, Fe, O elements. There was no additional peak observed which depicts the purity of the sample. The obtained atomic percentage of elements Co, Zn, Fe and O were found to be 11.87%, 4.92%, 31.23% and 51.98%. It is well matched with the stoichiometric proportion of components in prepared nanoparticles.

3.2 Raman spectra study

Figure 3 shows the Raman spectra of prepared CZF NPs recorded within the 100 cm^{-1} to 800 cm^{-1} frequency range at room temperature. Based on the Lorentzian function, Raman spectra were fitted by the best-fitting procedure. According to group theory A_{1g}, E_g and $3T_{2g}$ five Raman active modes out of 39 vibrational modes were generated in spinel ferrites [25]. In the Raman spectra of spinel ferrite; peaks below and above 600 cm^{-1} frequency indicated the octahedral and tetrahedral sites respectively. The Raman spectra of the prepared CZF sample show two A_{1g}, one E_g and three T_{2g} modes shown in Table 3. The A_{1g} is the higher frequency mode which indicates the symmetric stretching of M−O at the tetrahedral site. In the case of the present Raman spectra $A_{1g}(1)$ and $A_{1g}(2)$ modes were observed, this is maybe due to the redistribution of Fe−O and Co−O bond distance at both sites because of the difference in ionic radii. E_g and T_{2g} modes observed below 600 cm^{-1} frequency are also known as low-frequency phonon modes. E_g mode credited due to the symmetric bending of O-M and $T_{2g}(3)$ due to the asymmetric bending of oxygen to metal ion at the octahedral site. $T_{2g}(1)$ mode is attributed due to the asymmetric bending of oxygen ion and $T_{2g}(2)$ mode attributed due to the asymmetric stretching's of oxygen ion at the octahedral site. The six modes that is $T_{2g}(1)$, E_g, $T_{2g}(2)$, $T_{2g}(3)$, $A_{1g}(2)$ and $A_{1g}(1)$ were observed having peak maxima at 189.13 cm^{-1}, 308.5 cm^{-1}, 466.40 cm^{-1}, 554.93 cm^{-1}, 616.74 cm^{-1} and 687.0 cm^{-1} respectively for prepared CZF sample.

Fig. 3
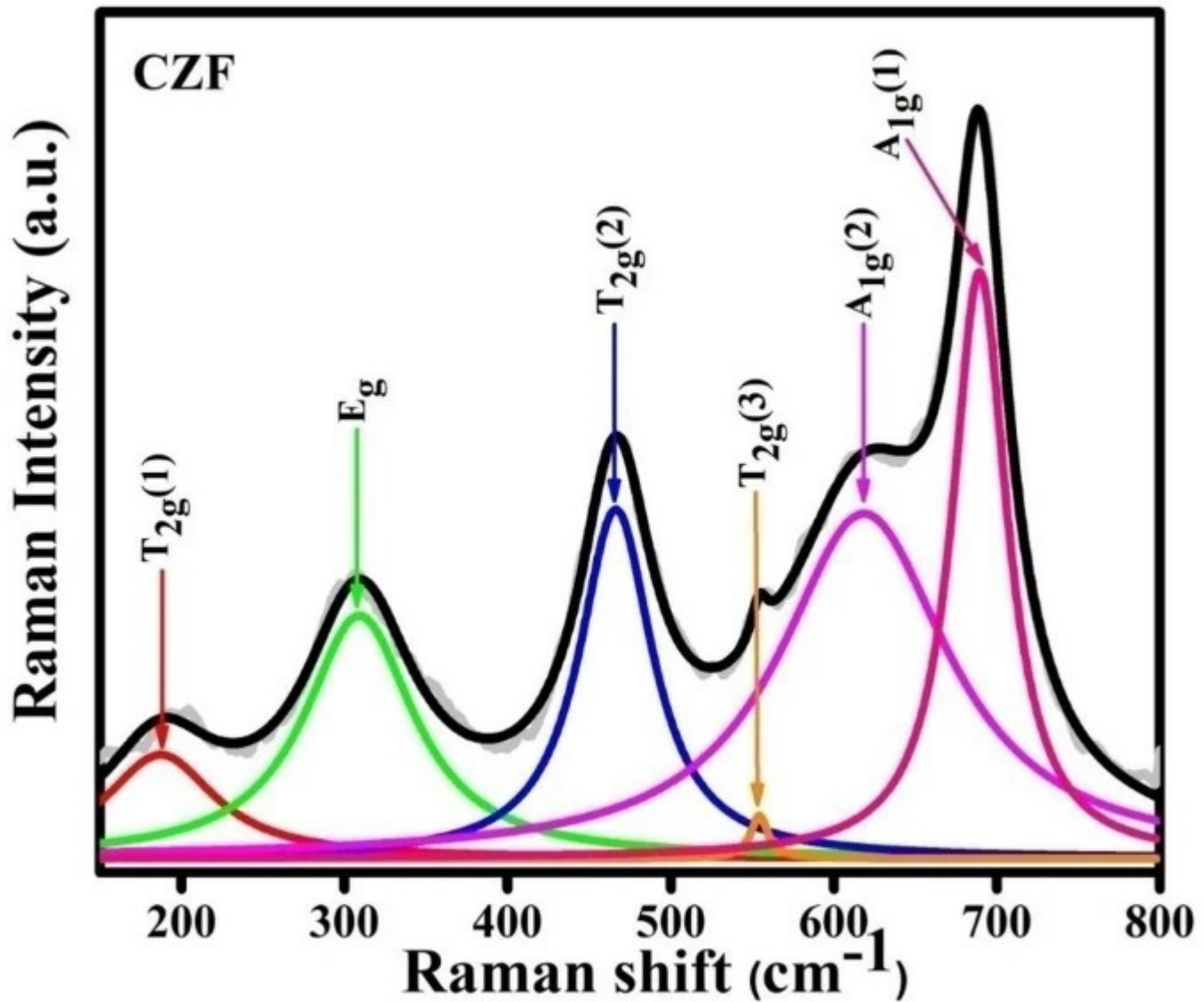
Best-fitting of Raman spectra for CZF in the range $100-800$ cm^{-1}

Table 3 Raman active modes for the CZF sample

3.3 Fourier transform infrared spectra (FTIR) study

The FTIR transmittance spectra of prepared both CZF and PEG-CZF samples recorded at room

temperature within the wavenumber range 300 cm^{-1} to 4000 cm^{-1} for the investigation of vibrational active modes are shown in Fig. 4. The vibrational modes present between the 300–600 cm^{-1} wavenumber range confirm the formation of the spinel structure; these modes are observed in both samples. In the case of CZF sample v_1 mode and v_2 mode was observed at 568.76 cm^{-1} and 410.83 cm^{-1}, respectively, and in the case of PEG–CZF sample v_1 mode and v_2 mode was observed at 554.06 cm^{-1} and 400.97 cm^{-1}, respectively. The v_1 is a higher frequency mode that indicates the stretching vibration at the tetrahedral site and v_2 is a lower frequency mode that indicates the stretching vibration at the octahedral site. Excepting these two modes, PEG–CZF sample FT–IR spectra show additional modes at 1093 cm^{-1}, 1621 cm^{-1} and 3437 cm^{-1}. The band observed at 3437 cm^{-1} indicated the O−H bond which is also known as a structural bond. The peak that appeared at 1621 cm^{-1} is due to the asymmetric vibration of a carboxyl group (-COOH). The 1093 cm^{-1} is attributed due to the stretching vibration of the O−H bond. All these observed vibrational modes confirmed the appearance of the carboxylic group on the surface of PEG-CZF NPs which resulted from the successful coating of PEG over the core of CZF NPs. All results are well-matched with a previous report [26].

Fig. 4
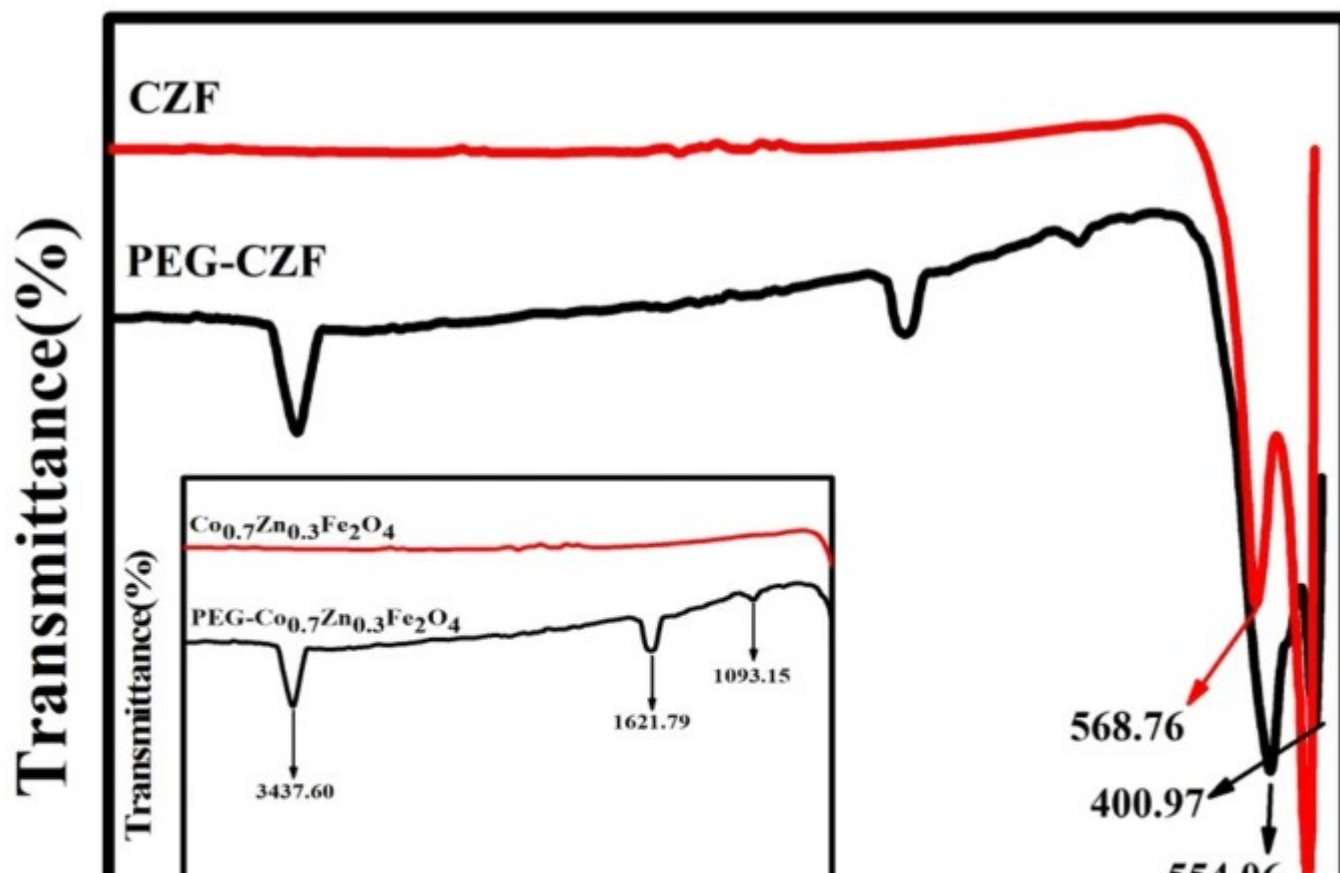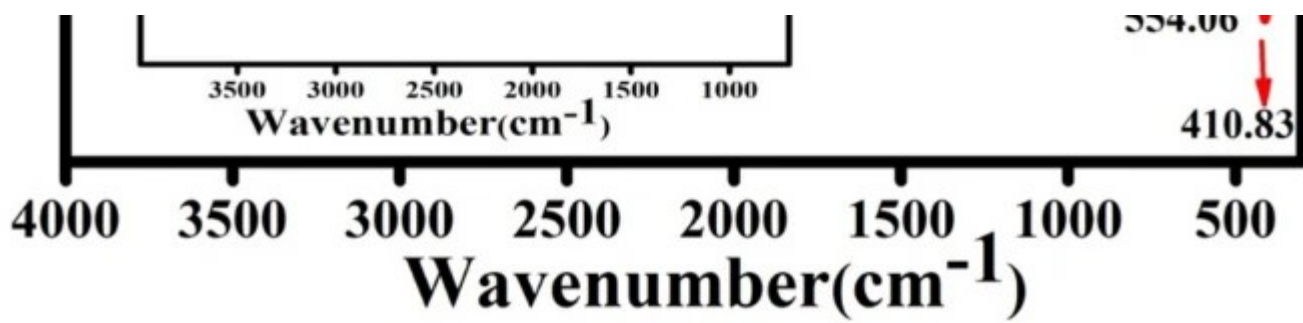
FTIR spectra of CZF and PEG–CZF samples

3.4 Morphology study

The morphology, particle size distribution, phase of structure and particle size determinations were investigated by using TEM. TEM image coupled with SAED pattern of CZF is shown in Fig. 5. The particles are non-uniform with having spherical nature was observed from the TEM image (Fig. 5a). The particles are highly agglomerated depicted in the TEM image. This is maybe due to the high magnetic dipole–dipole interaction of the particles which leads to the agglomeration of particles, similarly reported by Salunke et. al [27]. The average particle size calculated from the TEM image was found to be 31 nm which is in agreement with the crystallite size calculated from Reitveld refined XRD pattern. The particle size distribution was shown in the form of a histogram presented in Fig. 5b. SAED pattern of CZF NPs is shown in Fig. 5c. In the SEAD pattern, bright spots over the diffracted rings were observed. The concentric diffraction rings of planes having (h k l) values such as (220), (311), (400), (422) and (511) are characteristic diffraction planes of the cubic spinel structure, also similar planes obtained in reported XRD spectra. Similar results are also reported by Debnath et. al. on Co-doped Ni ferrite [28]. Thus, the formation of the cubic spinel structure of the prepared sample was confirmed.

Fig. 5
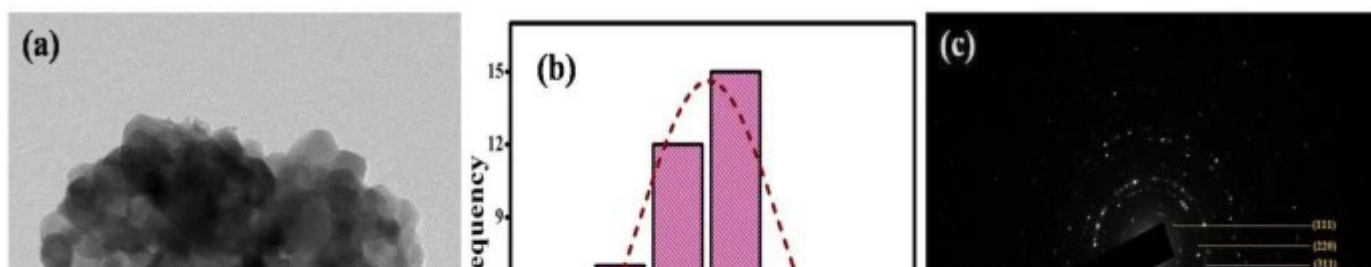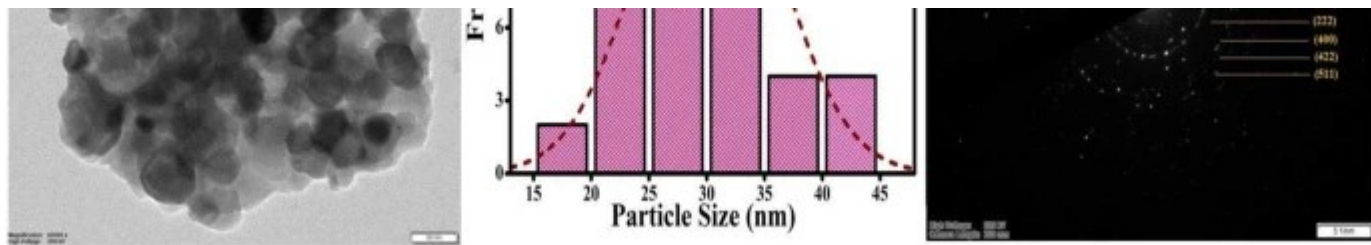
a TEM image, b histogram indicating the particle size distribution and c selected-area electron diffraction (SAED) of CZF

3.5 Contact angle (CA)

The effective use of magnetic materials in biomedical applications also depends on biocompatibility, stability and toxicity characteristics [29]. The hydrophilic nature of the sample shows good stability towards the base fluids such as water [30]. The wetting nature of the surface of the material can be calculated by using contact angle measurement. Modifying the surface chemistry of the core or the outermost layer of the specimen can easily change the CA of solid materials. The solid materials have two types of nature (hydrophilic and hydrophobic) depending on wetting characteristics. The hydrophilic and hydrophobic nature of materials can be specified by using contact angle measurement. The materials that have contact angles below 90° (contact angle $\leq$ 90°) which are hydrophilic in nature and materials have contact angles greater than 90° (contact angle $\geq$ 90°) which are hydrophobic in nature [31]. Figure 6 shows the contact angle images of PEG–CZF NPs.

Fig. 6
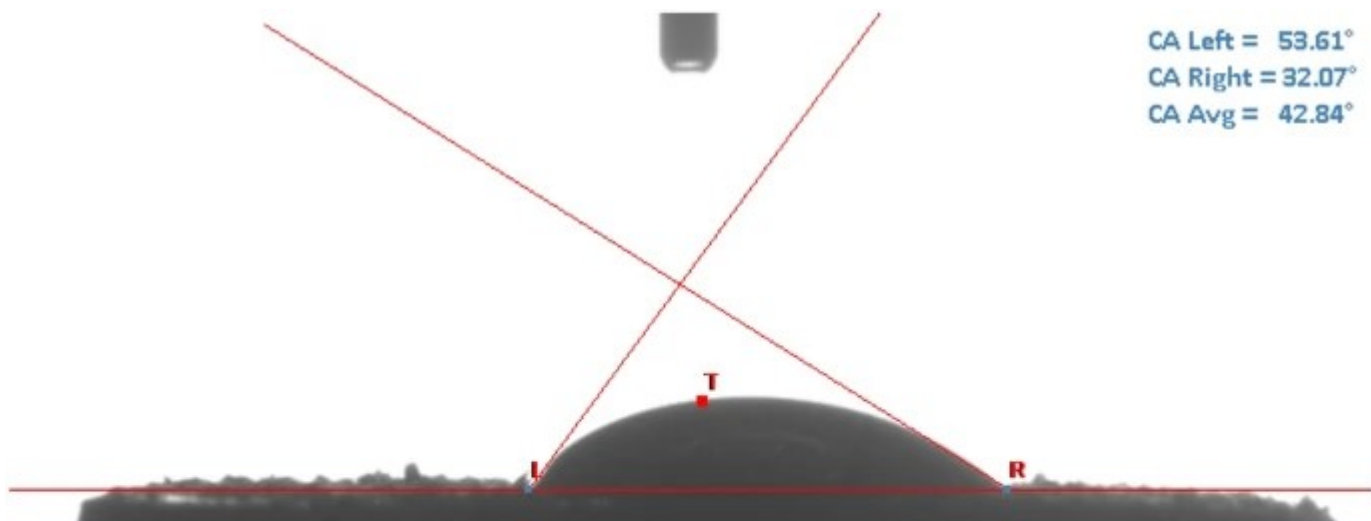
Water contact angle images of PEG-CZF

The contact angle of the PEG-CZF sample was found to be 42.84°. The obtained contact angle value is in good agreement with the value reported by Mushtaq et. al. for xanthan gum (XG) coated NPs [32]. The prepared sample has hydrophilic nature which is suitable for biomedical applications to improve the stability of fluids. The studied samples are coated samples. The coating of PEG on the surface of nanoparticles is responsible for less contact angle that is below 90°. The amphiphilic entities in PEG were presented on the surface of the nanoparticles which cover the core of nanoparticles.

3.6 Magnetic properties

3.6.1 M–H analysis

Magnetic nature and other magnetic parameters of prepared CZF and PEG-CZF NPs were investigated by M-H loops recorded at room temperature in applied magnetic fields of ± 30 kOe. The M-H loops of both samples are displayed in Fig. 7. The magnetic parameters like remanence magnetization (M_r), Saturation magnetization (M_s), remanence ratio (M_r/M_s) and magneton number were calculated from the M-H loop and tabulated in Table 4. The high saturation magnetization and low coercivity are characteristic of superparamagnetism. Both samples have high saturation magnetization with very low coercivity, therefore both samples have superparamagnetic nature at room temperature. The saturation magnetization of CZF and PEG-CZF NPs were found at 46.82 emu/g and 42.49 emu/g respectively. The saturation magnetization was observed to decrease after coating. The coercivity of prepared samples also observed to decrease after coating i.e. calculated coercivity of CZF and PEG-CZF NPs was 190.89 Oe and 57.60 Oe respectively. The magneton number was calculated by using Eq. 7 and

the magneton number also decreased after coating.

$$ n_{B} = \frac{{\left[{M_{s} \times M_{w} } \right]}}{5585} $$

(7)

where M_s is the saturation magnetization and M_w is the molecular mass of the sample [33]. From Table 4 it was observed that all magnetic parameters slightly decreased after coating with PEG. This happened may be due to reduced (A)−[B] interaction. The reduction of the particle−particle interface occurs due to PEG content which affects the (A)−[B] interaction. This result is in well consistent with previous reports [22]. The M–H loops of both samples were shows superparamagnetic natures at room temperature. The nanoparticles have superparamagnetic nature which is an essential condition for their use in biomedical applications. Therefore, the prepared samples are promising materials for biomedical applications, especially for magnetic hyperthermia applications.

Fig. 7

| -30000 | -15000 | 0 | 15000 | 30000 |

Magnetic Field (Oe)
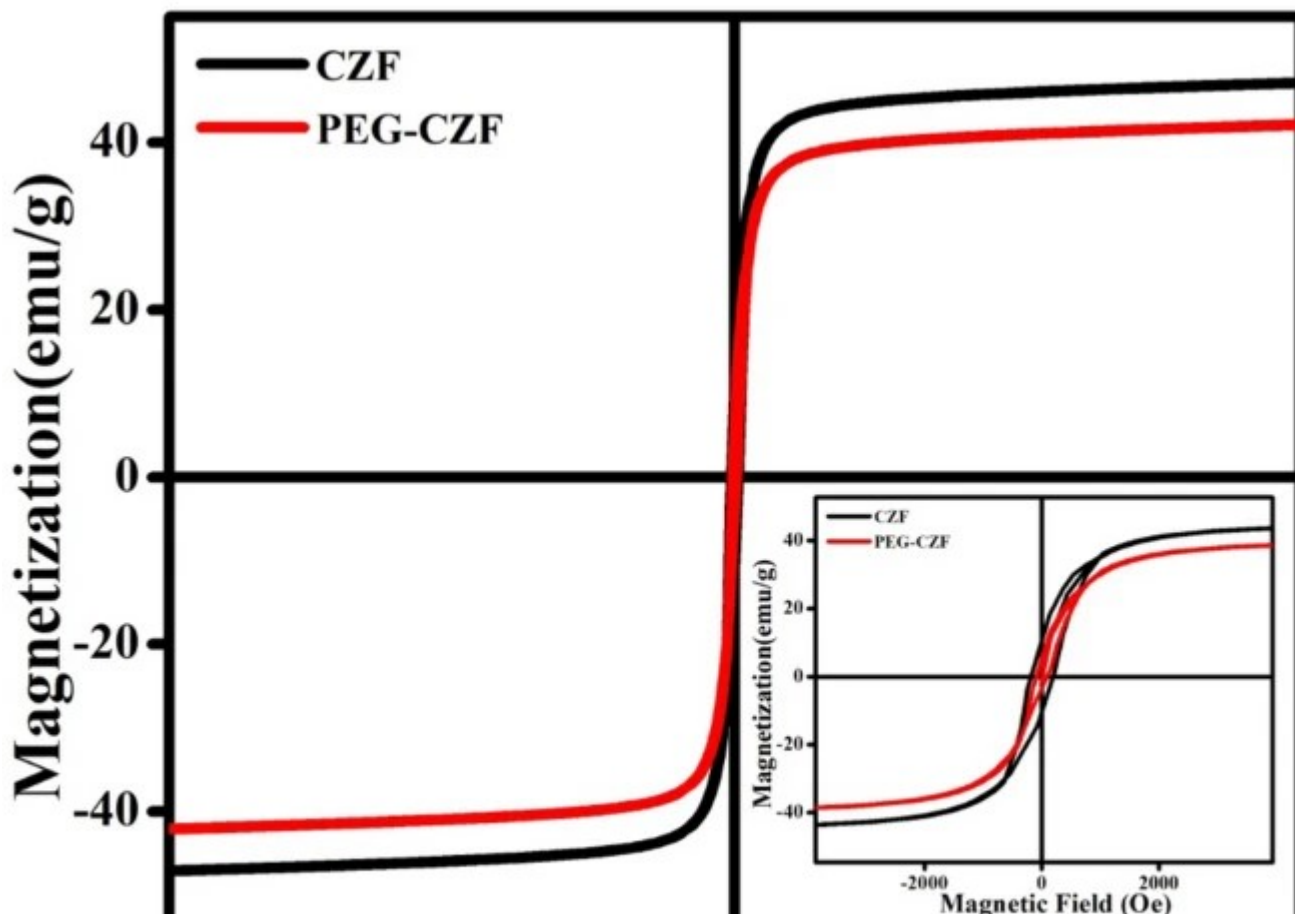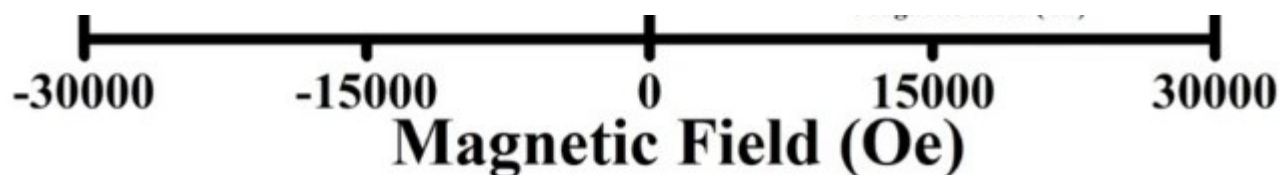
Room temperature Magnetic Hysteresis loop of CZF and PEG–CZF sample

Table 4 Magnetic parameters values; saturation magnetization (M_s), Coercivity (H_c), Remanence magnetization (M_r), Remanence ratio (M_r / M_s) and magneton number (n_B) calculated from the M−H loop of CZF and PEG–CZF

3.6.2 M–T analysis

Figure 8 depicts the FC-ZFC curve of CZF sample recorded under an applied magnetic field 500 Oe between the temperature range 20 to 350 K. Initially, NPs were cooled up to a low temperature (20 K) without applying any external magnetic field then in the presence of external magnetic field (500 Oe) the magnetization was recorded by increasing temperature up to 350 K, the obtained curve is known as zero field cooled (ZFC). After that the NPs were cooled down up to 20 K with an applied magnetic field (500 Oe), the magnetization was recorded for decreasing temperature which is known as the field cooled (FC) curve. In the case of the ZFC curve maximum magnetization was obtained at a specific temperature called the blocking temperature (T_B). The obtained blocking temperature from the FC–ZFC curve was 228 K. The magnetization decreased after blocking temperature and is clearly observed in the present FC-ZFC curve, which is the characteristic of the superparamagnetic nature of the particles. The FC and ZFC curve split from each other at a specific temperature known as the irreversibility temperature (T_{irr}). The irreversibility temperature was found to be 272 K for the CZF sample. With blocking temperature TB < 300 K, the CZF sample exhibit superparamagnetic behaviour. Similar result was reported by Pazik et. al. [34].

Fig. 8

80
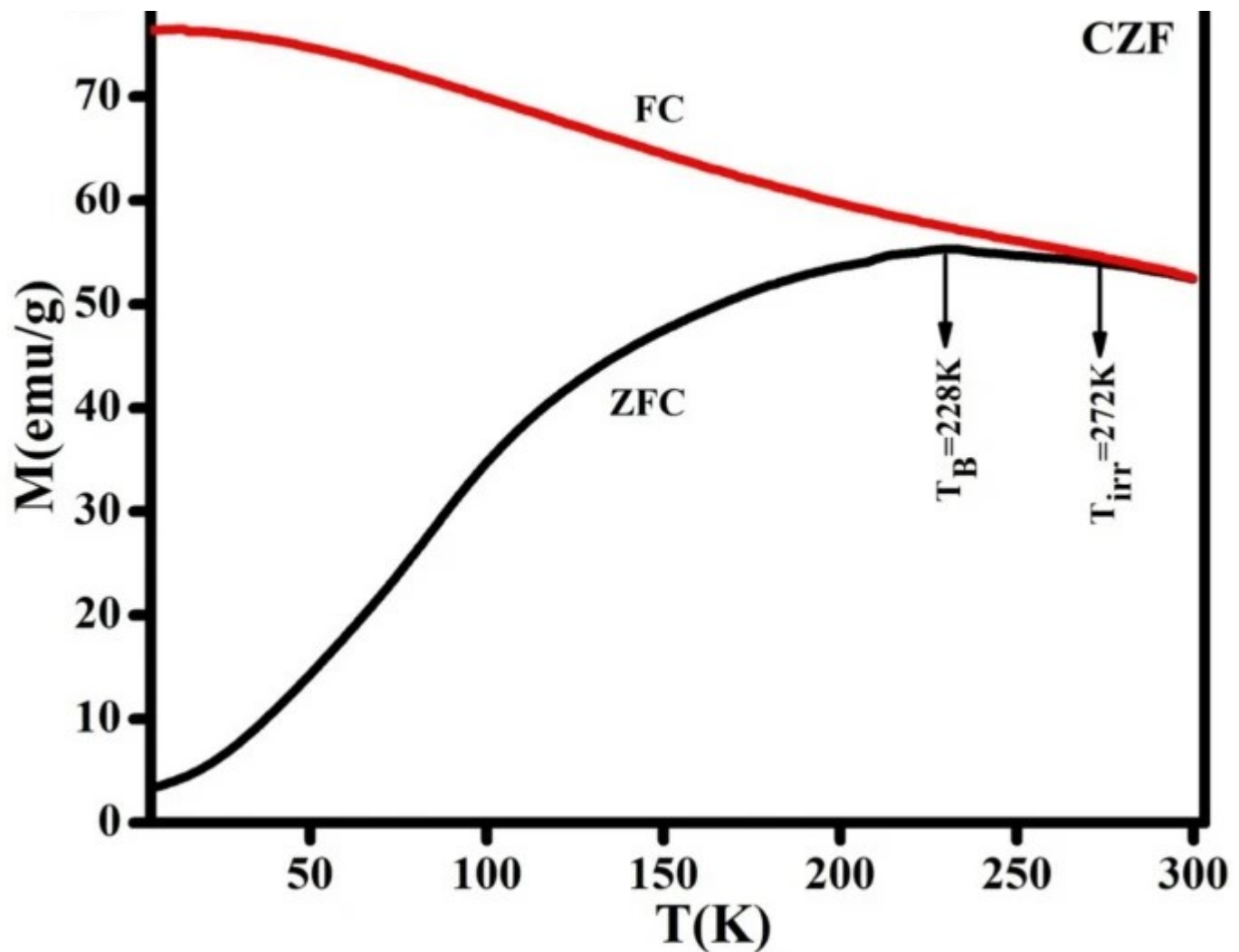
FC–ZFC curves of CZF sample under applied magnetic field 500 Oe

3.7 Magnetic hyperthermia study

The magnetic nanofluids with various concentrations of particles were prepared for the study of the magneto-thermal effects of prepared CZF and PEG-CZF NPs. The prepared NPs having concentrations 2 mg/mL, 4 mg/mL, 6 mg/mL, 8 mg/mL and 10 mg/mL were dispersed in water by ultrasonication for 4 h to obtain perfect nanofluids. The nanofluids were used for further induction heating analysis. The samples should achieve temperatures between 42 ⁰C and 45 ⁰C an essential condition for magnetic hyperthermia application [35]. Thus, the systematic magnetic hyperthermia application analysis of prepared CZF and PEG-CZF NPs was evaluated by the induction heating system. Figure 9 shows the induction heating curves of CZF and PEG-CZF NPs which were recorded at a frequency of 280 kHz with 35 kA/m applied magnetic field. From curves, as the time increased temperature increased sharply with

respect to the time but at the particular maximum level temperature it was saturated which is depicted in all curves. In the case of the CZF sample, the curves for 6 mg/mL and 4 mg/mL concentration NPs saturated nearly at 45 °C and 43 °C respectively which are exactly in the required range of hyperthermic temperature but curves for 2 mg/mL, 8 mg/mL and 10 mg/mL concentration of NPs saturated at 41 °C, 48 °C and 50 °C which are not in range for hyperthermic temperature. In the case of the PEG–CZF sample, three curves show saturated temperatures in the hyperthermic temperature range for curves of 4 mg/mL, 6 mg/mL and 8 mg/mL concentrations at 43 °C, 44 °C and 45 °C, respectively. The curves for 2 mg/mL and 10 mg/mL concentration, samples were saturated at 40 °C and 47 °C well below and above the hyperthermic temperature range. The PEG–CZF sample shows decreased temperature compared to the CZF sample for the same concentration extent graphically shown in Fig. 10a, which can be attributed to PEG coating on the surface of the particles that reduces the magnetic properties [36]. The initial increased temperature with time (dT/dt) for all concentrations of both samples are plotted comparatively, depicted in Fig. 10b. The saturation temperature and initial stage slope of temperature versus time were found to be linear to the concentration of NPs, clearly observed in Fig. 10. Similarly, a comparative study was reported by Yousaf et. al. [37] for silica–coated iron oxide NPs. The heating property of magnetic samples was affected by several factors such as particle size, magnetization, etc. The heat rise in the NPs depends on the applied external magnetic field. This mechanism arises due to magnetic losses known as 'hysteresis losses' and 'relaxation losses'. But the magnetic study revealed both samples have superparamagnetic nature with negligible coercivities (191 and 58 Oe). Thus, hysteresis losses can be clearly ignored in the superparamagnetic case. The relaxation losses were further classified into two losses; Neel losses and Brownian losses. The physical rotation of particles in an aqueous medium is attributed to Brownian losses, thus in the present case thermal rise may arise due to Brownian losses.
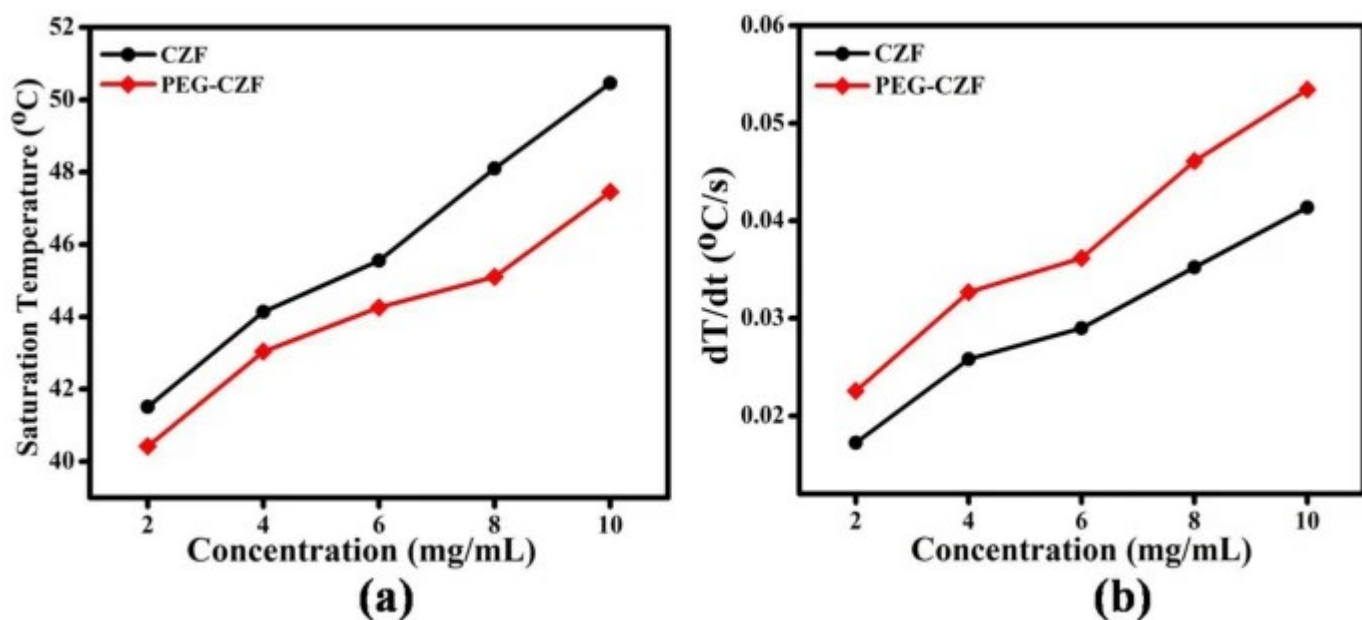
Fig. 9
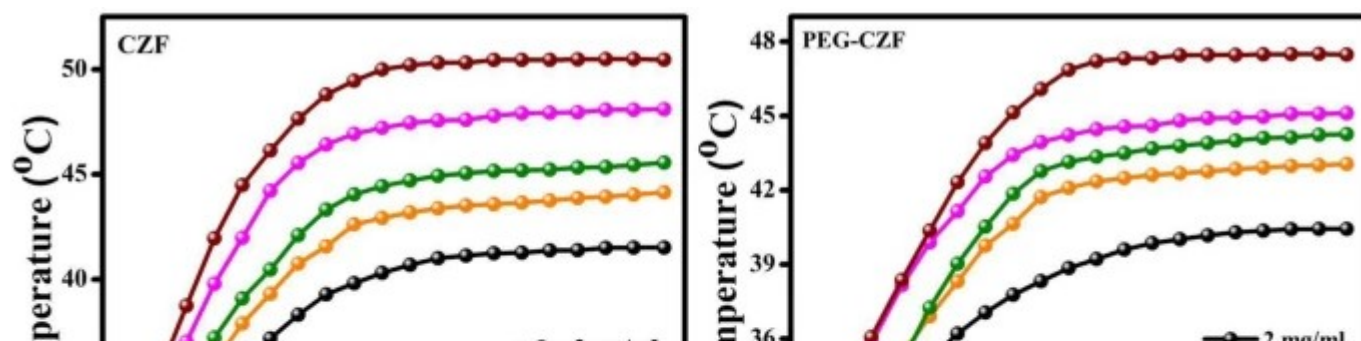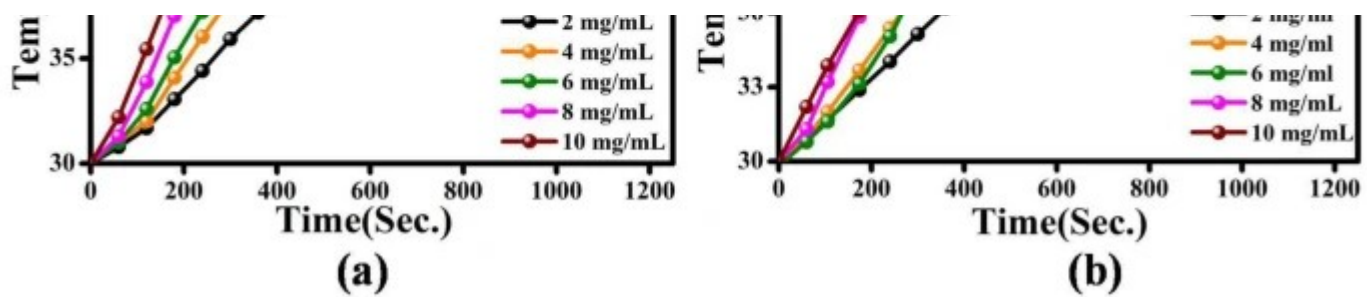
Induction heating curve of CZF and PEG–CZF NPs for different particle concentration

Fig. 10

a Saturation temperature with respect to concentration and b Concentration versus an average temperature rise with a time of CZF and PEG–CZF sample

### 3.7.1 Specific absorption rate analysis (SAR)

The heating capacity of particles is analyzed by measuring the SAR value. The heat generated per unit mass of the magnetic NPs is known as SAR [1]. In the presence of an external magnetic field, NPs produce thermal heat due to the magnetic moment of particles. SAR is the most impressive and effective parameter in induction heating study. In the present study, the value of SAR is calculated from the equation

$$ {\text{SAR }} = C \times {\raise0.7ex\hbox{${dT}$} \!\mathord{\left/ {\vphantom {{dT} {dt}}}\right.\kern-\nulldelimiterspace} \!\lower0.7ex\hbox{${dt}$}} \times {\raise0.7ex\hbox{${M_{s} }$} \!\mathord{\left/ {\vphantom {{M_{s} } {M_{m} }}}\right.\kern-\nulldelimiterspace} \!\lower0.7ex\hbox{${M_{m} }$}} $$

(8)

where C is the specific heat capacity of the sample, dT/dt is the initial stage slope of temperature versus time plot, M_s is the mass of the total sample and M_m is the magnetic content mass in the sample. Figure 11 (a−b) shows the plots of SAR values for both CZF and PEG–CZF samples with respect to concentration. The SAR values of the CZF sample were found to be 108.15 W/g, 134.98 W/g, 141.54 W/g, 165.79 W/g and 166.89 W/g for 2, 4, 6, 8 and 10 mg/mL concentrations, respectively. In the case of the PEG–CZF sample, the values of SAR were obtained at 141.46 W/g, 170.93 W/g, 176.65 W/g, 217.12 W/g and 246.09 W/g for 2, 4, 6, 8 and 10 mg/mL concentration, respectively. The values of SAR parameters were found to be increased with increasing NPs concentration in base fluids (water). In addition, PEG–coated sample (i.e. PEG–CZF) shows superior SAR values as compared to the uncoated sample (i. e. CZF), this may be due to particle size and magnetic saturation of prepared nanoparticles which are two important parameters in magnetic hyperthermia study [38]. Therefore the prepared sample is more applicable for magnetic hyperthermia biomedical application.

Fig. 11
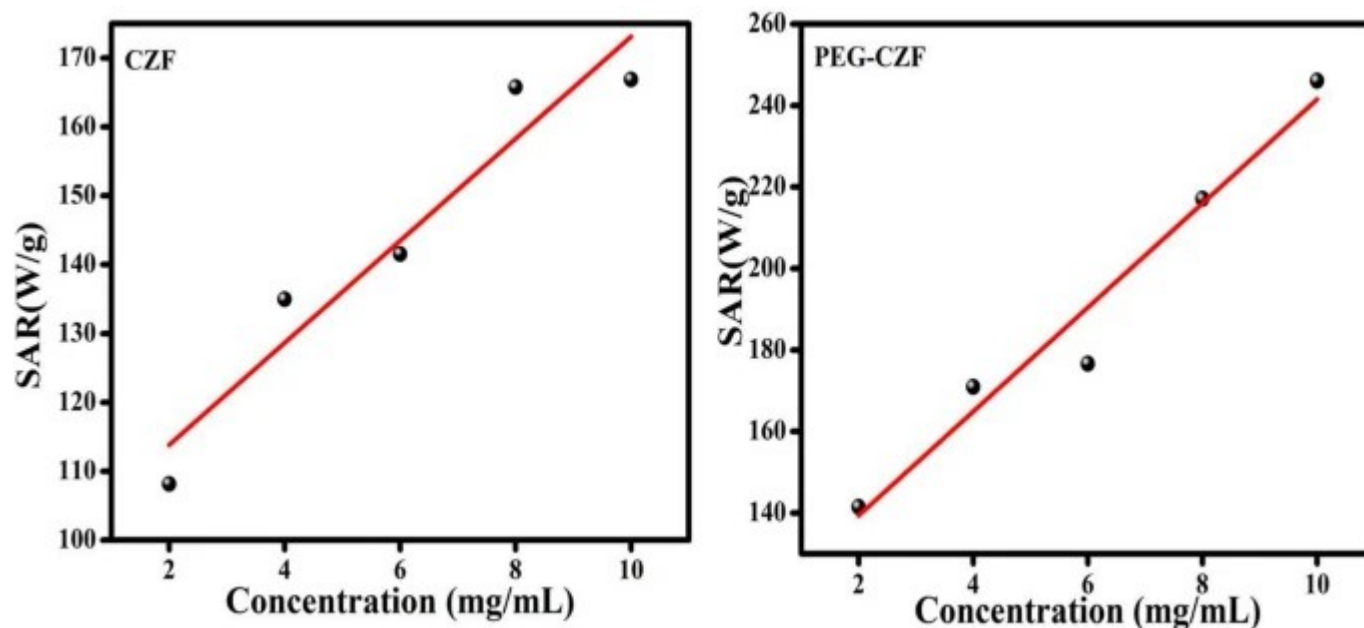
(a)   **(b)**

Variation of specific absorption rate (SAR) with respect to the concentration of CZF (a) and PEG-CZF (b)

4 Conclusion

Co-Zn spinel ferrite NPs with enhanced structural, chemical and magnetic properties were successfully prepared by the chemical co-precipitation method. The XRD study revealed the formation of FCC structure with nanocrystalline nature having crystallite size 23–24 nm. Calculated crystallite size from both W–H plots and Rietveld refinement were found to be closely similar. The characteristic spinel ferrite Raman modes (A_{1g}, E_g and $3T_{2g}$) were present in Raman spectra which revealed the formation of spinel ferrite. The presence of Raman modes in Raman spectra confirmed the formation of spinel ferrite. The spinel phase of NPs and PEG coating on the surface of NPs was confirmed from frequency-vibrational modes observed in FTIR spectra. The nanocrystalline nature with 31 nm particle size was confirmed from the TEM image and SAED pattern. The magnetic study revealed that both CZF and PEG–CZF samples have superparamagnetic nature. The prepared sample has hydrophilic nature which is suitable for biomedical applications to improve the stability of fluids. Coated samples show improved hyperthermic properties as compared to uncoated samples. The concentration dependence study indicates that hyperthermic temperature increases from 42 to 45 °C as increasing dose rate. However, coated sample shows better results as compared to the uncoated sample. Further at a high concentration dose (10 mg/mL) in both cases (CZF and PEG-CZF) the temperature goes beyond the normal range of hyperthermic temperature. The PEG-CZF sample shows superior SAR values as compared to CZF sample. The prepared NPs can be used in hyperthermia applications for cancer treatment and would also be useful in other applications in the biomedical field.

References

1. A. Ahmad, H. Bae, C. Kim, I. Rhee, Characterization of zinc-doped cobalt ferrite

nanoparticles for application as heat generators in magnetic hyperthermia and MRI contrast agents. J. Korean Phys. Soc. 74(12), 1151–1159 (2019)

Article   ADS   Google Scholar

2. S.A. Jadhav, S.B. Somvanshi, M.V. Khedkar, S.R. Patade, K. Jadhav, Magneto-structural and photocatalytic behavior of mixed Ni−Zn nano-spinel ferrites: visible light-enabled active photodegradation of rhodamine B. J. Mater. Sci.: Mater. Electron. 31, 11352−11365 (2020)

Google Scholar

3. D.D. Andhare, S.R. Patade, J.S. Kounsalye, K. Jadhav, Effect of Zn doping on structural, magnetic and optical properties of cobalt ferrite nanoparticles synthesized via. Co-precipitation method. Physica B Condensed Matter 583, 412051 (2020)

Article   Google Scholar

4. H.-G. Wang, J.-W. Li, X.-T. Huo, C.-S. Yue, B. Peng, M. Zhang, M. Guo, Magnetic Ni-Zn spinel ferrite nanopowder from toxic Zn-bearing electric arc furnace dust: A promising treatment process. Miner. Eng. 157, 106540 (2020)

Article   Google Scholar

5. O. Cadar, T. Dippong, M. Senila, E.-A. Levei, Progress, Challenges and opportunities in divalent transition metal-doped cobalt ferrites nanoparticles applications. Adv. Funct. Mater. IntechOpen. 1−17 (2020)

6. S. Amiri, H. Shokrollahi, The role of cobalt ferrite magnetic nanoparticles in medical science. Mater. Sci. Eng., C 33(1), 1−8 (2013)

Article   Google Scholar

7. T. Tatarchuk, M. Bououdina, J.J. Vijaya, L.J. Kennedy. Spinel ferrite nanoparticles: synthesis, crystal structure, properties, and perspective applications. in International Conference on Nanotechnology and Nanomaterials. Springer (2016)

8. G. Katoch, G. Rana, M. Singh, A. García-Peñas, S. Bhardwaj, I. Sharma, P. Sharma, G. Kumar, Recent advances in processing, characterizations and biomedical applications of spinel ferrite nanoparticles. Ferrite 112 62–120 (2021)

9. V. Bhagwat, M.V. Khedkar, G. Kulkarni, P.B. Kharat, K. Jadhav. Dextrose assisted sol-gel auto combustion synthesis and magnetic characterizations of cobalt ferrite nanoparticles. in AIP Conference Proceedings. AIP Publishing LLC (2020)

10. Y. Huang, S. He, W. Cao, K. Cai, X.-J. Liang, Biomedical nanomaterials for imaging-guided cancer therapy. Nanoscale 4(20), 6135–6149 (2012)

Article   ADS   Google Scholar

11. A. Szasz, N. Szasz, O. Szasz, Hyperthermia results and challenges, in *Oncothermia: Principles and Practices*. (Springer, 2010), pp. 17–88

Chapter   Google Scholar

12. P. Wust, B. Hildebrandt, G. Sreenivasa, B. Rau, J. Gellermann, H. Riess, R. Felix, P. Schlag, Hyperthermia in combined treatment of cancer. Lancet Oncol. 3(8), 487–497 (2002)

Article   Google Scholar

13. M.W. Dewhirst, B. Viglianti, M. Lora-Michiels, M. Hanson, P. Hoopes, Basic principles of thermal dosimetry and thermal thresholds for tissue damage from hyperthermia. Int. J. Hyperth. 19(3), 267–294 (2003)

Article   Google Scholar

14. P. Cherukuri, E.S. Glazer, S.A. Curley, Targeted hyperthermia using metal nanoparticles. Adv. Drug Deliv. Rev. 62(3), 339–345 (2010)

Article   Google Scholar

15. S. Tran, P.-J. DeGiovanni, B. Piel, P. Rai, Cancer nanomedicine: a review of recent success in drug delivery. Clin. Transl. Med. 6(1), 1–21 (2017)

Article   Google Scholar

16. R.R. Kahmei, J. Borah, Clustering of MnFe2O4 nanoparticles and the effect of field intensity in the generation of heat for hyperthermia application. Nanotechnology 30(3), 035706 (2018)

Article   Google Scholar

17. R. Raland, J. Borah, Efficacy of heat generation in CTAB coated Mn doped ZnFe2O4 nanoparticles for magnetic hyperthermia. J. Phys. D Appl. Phys. 50(3), 035001 (2016)

Article   ADS   Google Scholar

18. S.R. Patade, D.D. Andhare, S.B. Somvanshi, P.B. Kharat, S.D. More, K.M. Jadhav, Preparation and characterisations of magnetic nanofluid of zinc ferrite for hyperthermia. Nanomaterials and Energy 9(1), 8–13 (2020)

Article   Google Scholar

19. S. Halder, S. Liba, A. Nahar, S. Sikder, S.M. Hoque, To study the surface modified cobalt zinc ferrite nanoparticles for application to magnetic hyperthermia. AIP Adv. 10(12), 125308 (2020)

Article   ADS   Google Scholar

20. H. Choi, S. Lee, T. Kouh, S.J. Kim, C.S. Kim, E. Hahn, Synthesis and characterization of Co-Zn ferrite nanoparticles for application to magnetic hyperthermia. J. Korean Phys. Soc. 70(1), 89–92 (2017)

Article   ADS   Google Scholar

21. M.S. Darwish, H. Kim, H. Lee, C. Ryu, J.Y. Lee, J. Yoon, Synthesis of magnetic ferrite nanoparticles with high hyperthermia performance via a controlled co-precipitation method. Nanomaterials 9(8), 1176 (2019)

Article   Google Scholar

22. S.B. Somvanshi, P.B. Kharat, M.V. Khedkar, K. Jadhav, Hydrophobic to hydrophilic surface transformation of nano-scale zinc ferrite via oleic acid coating: magnetic hyperthermia study towards biomedical applications. Ceram. Int. 46(6), 7642–7653 (2020)

Article   Google Scholar

23. S. Nosheen, M. Irfan, S.H. Abidi, Q. Syed, F. Habib, A. Asghar, B. Waseem, B. Soomro, H. Butt, M. Akram, A review: Development of magnetic nano vectors for biomedical applications. GSC Adv. Res. Rev. 8(2), 085–110 (2021)

Article   Google Scholar

24. A. Younes, N. Kherrouba, A. Bouamer, Magnetic, optical, structural and thermal properties of copper ferrite nanostructured synthesized by mechanical alloying. Micro & Nano Letters 16(4), 251–256 (2021)

Article   Google Scholar

25. D.D. Andhare, S.R. Patade, S.A. Jadhav, S.B. Somvanshi, K. Jadhav, Rietveld refined structural, morphological, Raman and magnetic investigations of superparamagnetic Zn–Co nanospinel ferrites prepared by cost-effective co-precipitation route. Appl. Phys. A 127(6), 1–13 (2021)

Article   Google Scholar

26. T. Zargar, A. Kermanpur, S. Labbaf, A.B. Houreh, M.N. Esfahani, PEG coated Zn0 3Fe2 7O4 nanoparticles in the presence of< alpha Fe2O3 phase synthesized by citric acid assisted hydrothermal reduction process for magnetic hyperthermia applications. Mater. Chem. Phys. 212, 432–439 (2018)

27. A. Salunkhe, V. Khot, N. Thorat, M. Phadatare, C. Sathish, D. Dhawale, S. Pawar, Polyvinyl alcohol functionalized cobalt ferrite nanoparticles for biomedical applications. Appl. Surf. Sci. 264, 598–604 (2013)

Article   ADS   Google Scholar

28. S. Debnath, A. Das, R. Das, Effect of cobalt doping on structural parameters, cation distribution and magnetic properties of nickel ferrite nanocrystals. Ceram. Int. 47(12), 16467–16482 (2021)

Article   Google Scholar

29. A.K. Gupta, M. Gupta, Synthesis and surface engineering of iron oxide nanoparticles for biomedical applications. Biomaterials 26(18), 3995–4021 (2005)

Article   Google Scholar

30. D.S. Mathew, R.-S. Juang, An overview of the structure and magnetism of spinel ferrite nanoparticles and their synthesis in microemulsions. Chem. Eng. J. 129(1–3), 51–65 (2007)

Article   Google Scholar

31. J. Yirijoh, Surface Modification of Polymeric Biomaterials for Cell/Tissue Integration. (2016)

32. M.W. Mushtaq, F. Kanwal, A. Islam, K. Ahmed, Z.-U. Haq, T. Jamil, M. Imran, S.M. Abbas, Q. Huang, Synthesis and characterisation of doxorubicin-loaded functionalised cobalt ferrite nanoparticles and their in vitro anti-tumour activity under an AC-magnetic field. Trop. J. Pharm. Res. 16(7), 1663–1674 (2017)

Article   Google Scholar

33. A. Anwar, M.A. Yousuf, S. Zulfiqar, P.O. Agboola, I. Shakir, N.F. Al-Khalli, M.F. Warsi, The impact of highly paramagnetic Gd3+ cations on structural, spectral, magnetic and dielectric properties of spinel nickel ferrite nanoparticles. J. Saudi Chem. Soc. 25(9), 101306 (2021)

Article   Google Scholar

34. R. Pązik, A. Zięcina, E. Zachanowicz, M. Małecka, B. Poźniak, J. Miller, Z. Śniadecki, N. Pierunek, B. Idzikowski, L. Mrówczyńska, Synthesis, structural features, cytotoxicity, and magnetic properties of colloidal ferrite spinel $Co_{1-x}Ni_xFe_2O_4$ ($0.1 \leq x \leq 0.9$) Nanoparticles. Eur. J. Inorgan. Chem. 2015(28), 4750–4760 (2015)

Article   Google Scholar

35. M.A. Kerroum, A. Essyed, C. Iacovita, W. Baaziz, D. Ihiawakrim, O. Mounkachi, M. Hamedoun, A. Benyoussef, M. Benaissa, O. Ersen, The effect of basic pH on the elaboration of $ZnFe_2O_4$ nanoparticles by co-precipitation method: Structural, magnetic and hyperthermia characterization. J. Magn. Magn. Mater. 478, 239–246 (2019)

Article   ADS   Google Scholar

36. V. Khot, A. Salunkhe, N. Thorat, R. Ningthoujam, S. Pawar, Induction heating studies of dextran coated $MgFe_2O_4$ nanoparticles for magnetic hyperthermia. Dalton Trans. 42(4), 1249–1258 (2013)

Article   Google Scholar

37. Y. Iqbal, H. Bae, I. Rhee, S. Hong, Intensive analysis of core–shell silica-coated iron-oxide nanoparticles for magnetic hyperthermia. J. Nanosci. Nanotechnol. 16(11), 11862–11867 (2016)

Article   Google Scholar

38. A. Rezanezhad, A. Hajalilou, F. Eslami, E. Parvini, E. Abouzari-Lotf, B. Aslibeiki, Superparamagnetic magnetite nanoparticles for cancer cells treatment via magnetic hyperthermia: effect of natural capping agent, particle size and concentration. J. Mater. Sci.: Mater. Electron. 32(19), 24026–24040 (2021)

Google Scholar

Acknowledgements

Author information

Authors and Affiliations

Department of Physics, Dr. Babasaheb Ambedkar, Marathwada University, Aurangabad, 431004, Maharastra, India

Deepali D. Andhare, Supriya R. Patade, Mangesh V. Khedkar, Asha A. Nawpute & K. M. Jadhav

Corresponding author

Correspondence to [Deepali D. Andhare](#).

Ethics declarations

Conflicts of interest

There are no conflicts of interest connected to the present work.

Additional information

Publisher's Note

Springer Nature remains neutral with regard to jurisdictional claims in published maps and institutional affiliations.

Rights and permissions

[Reprints and permissions](#)

About this article

Share this article

Anyone you share the following link with will be able to read this content:

Get shareable link

Provided by the Springer Nature SharedIt content-sharing initiative